MJO Initiation Westward Shifted and Propagation Blocked under Indian Ocean Basin Warming during Boreal Summer

Yuwen Wang[123], Hong-Li Ren[123], Yuntao Wei[1], Jie Wu[4], Shuo Zhao[1] and Wenwen Xu[5]

[1]Department of Atmospheric and Oceanic Sciences and Institute of Atmospheric Sciences, CMA-FDU Joint Laboratory of Marine Meteorology, Key Laboratory of Polar Atmosphere-ocean-ice System for Weather and Climate, Ministry of Education, Fudan University, Shanghai 200438, China.

[2]Collaborative Innovation Center on Forecast and Evaluation of Meteorological Disasters (CIC-FEMD), Nanjing University of Information Science and Technology, Nanjing 210044, China.

[3]State Key Laboratory of Severe Weather, and Institute of Tibetan Plateau Meteorology, Chinese Academy of Meteorological Sciences, Beijing, China.

[4]China Meteorological Administration Key Laboratory for Climate Prediction Studies, National Climate Center, Beijing, China.

[5]College of Aviation Meteorology, Civil Aviation Flight University of China, Guanghan, China.

Corresponding author: Hong-Li Ren (renhl@cma.gov.cn)

Key Points:

- Influences of the boreal summer Indian Ocean basin warming and cooling on the Madden-Julian Oscillation (MJO) are significantly distinct
- The Indian Ocean basin warming causes more westward-shifted MJO initiation and confines the MJO propagation within the basin
- The premoistening from synoptic-scale meridional moisture advection is key for MJO propagating eastward during boreal summer

Abstract

The Madden-Julian Oscillation (MJO) exhibits evident interannual variations, which have been mostly attributed to modulations of El Niño-Southern Oscillation (ENSO) in previous studies. However, whether the basin-wide warming/cooling of the Indian Ocean (IO) independent of ENSO could affect the MJO remains elusive. Here, we show that the MJO tends to initiate more westward and only propagate confined over the IO under warm conditions during boreal summer. In contrast, a cold IO results in an eastward-shifted MJO initiation and smooth propagation across the Maritime Continent (MC)-western Pacific (WP). The genesis location is mainly associated with warm ocean beneath the MJO, which accumulate more during warm conditions. Additionally, the warming of the IO induces anomalous anticyclone and stronger vertical wind shears over the WP, which synergistically lead to stronger Rossby wave while weaker Kelvin wave components, thereby inhibiting the MJO eastward propagation. Moreover, the suppressed convection and thus low-level Kelvin easterly wind anomalies over the MC-WP region become weaker with the warming of the entire IO. Consequently, the premoistening dominated by the high-frequency synoptic-scale meridional advection decreases and causes nonpropagating MJO during boreal summer. These findings highlight that interannual variations of the MJO could be attributed by considering independent modulation effects of the IO.

1 Introduction

The Madden–Julian oscillation (MJO; Madden & Julian, 1971, 1972) is one of the major modes of the tropical intraseasonal variability in the Indo-Pacific warm pool with a pronounced seasonality (Madden, 1986; Wei & Ren, 2024). The boreal winter MJO mainly propagates slowly eastward with large-scale deep convection along the equator, while the boreal summer

MJO moves both northward and eastward within the Asian monsoon zone (Yasunari, 1979; Wang & Rui, 1990; Madden & Julian, 1994; Jiang et al., 2004; Lin & Li, 2008; Wei et al., 2022). The MJO diabatic heating excites anomalous circulation that considerably modulates global weather and climate through teleconnections (Adames & Wallace, 2015; Ren & Ren, 2017; Bai et al., 2022). Deeply understanding the initiation and propagation MJO dynamics is thus important for the subseasonal-to-seasonal (S2S) prediction of meteorological disasters worldwide (Zhang, 2013; Vitart et al., 2017; Ren et al., 2018).

The year 2020 witnessed the wettest summer since 1960s over the Yangtse River basin, where a sequence of extreme rainfall episodes occurred, accompanied with a strengthened and westward extended western Pacific anticyclone (WPAC) (Ding et al., 2021). It was suggested that the unique MJO behaviors during June-July 2020 might affect the WPAC and thus the extreme Meiyu event (e.g., Zhang et al., 2021). As seen from Fig. 1a, the MJO recorded by the real-time multivariate MJO (RMM) index (Wheeler & Hendon, 2004; Ren et al., 2023) swung recurrently between Phases 1 and 2 in June-July when the westward extended ridge line of the WPAC also migrated southward or northward (Wang et al., 2022). Thus, the MJO stalling over the Indian Ocean and failing to propagate into the western Pacific was one cause of the persistent rainfall over the Yangtse River Basin in 2020. But why did the MJO stall in the early summer of 2020? We note that this special MJO episode followed a cooling condition in the central-eastern Pacific (Ding et al., 2021; Qiao et al., 2021; Zhang et al., 2021; Zhou et al., 2021) and also a warming condition persisting over the Indian Ocean (Figs. 1b–1c). This motivates that the anomalous oceanic conditions might play a role in affecting the MJO in 2020 summer. In fact, a preliminary study by Liang et al. (2021) has revealed that the non-propagating MJO during June-July 2020 might be associated with both a La Niña-like condition in the Pacific and an Indian

Ocean basin mode (IOBM)-like condition in the Indian Ocean, although underlying mechanisms remain elusive.

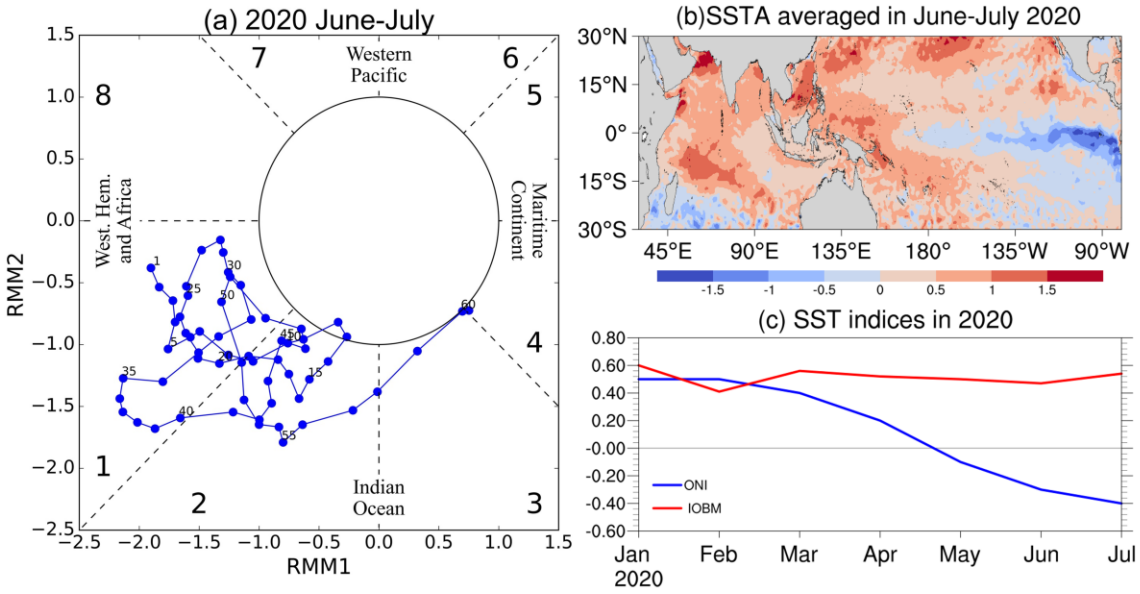

Figure 1. (a) The RMM indices during June–July 2020. (b) The sea surface temperature (SST) anomaly (units: ℃) averaged in June–July 2020. (c) The oceanic Niño index (ONI) and the Indian Ocean basin mode (IOBM) index during January–July 2020.

Many studies have tried to understand modulation effects of the El Niño-Southern Oscillation (ENSO) on the MJO (e.g., Lau & Chan 1986; Slingo et al., 1999; Hendon et al., 2007). The initiation and propagation behaviors of the MJO not only rely on the warm and cold phases of ENSO (Pohl & Matthews 2007; Liu et al., 2016) but are also subjected to the diverse spatial patterns of ENSO (Hsu & Xiao, 2017; Wang et al., 2019; Takasuka & Satoh, 2021). In general, the MJO becomes faster, bigger, and more top-heavy during El Niño than that during La Niña (Wei & Ren, 2019, 2022). The Central-Pacific El Niño supports successive MJO initiation from the Indian Ocean with a westward energy dispersion, while the Eastern-Pacific La Niña is favorable for the occurrence of primary MJO episodes triggered by westward-propagating Rossby waves (Wei et al., 2023).

Despite many studies on the ENSO-MJO interactions, potential effects of low-frequency sea surface temperature (SST) anomalies internal to the Indian Ocean (Cai et al., 2019; Wang, 2019) on the MJO are less investigated (Shinoda & Han, 2005; Seiki et al., 2015). During boreal summer, the anomalous Indian Ocean warming may slow and inhibit the northward propagation of the MJO (Sabeerali et al., 2013; Kottapalli & Vinayachandran, 2022). Although the IOBM exists as the dominant interannual variability mode over the Indian Ocean (Saji et al., 1999), few studies have examined whether it can influence the zonal propagation and initiation of boreal summer MJO, which largely motivates this study. For example, how does the MJO propagate in the warm versus cold phases of IOBM? Does the IOBM influence initiation of the MJO deep convection over the Indian Ocean? Addressing these questions is beneficial for the subseasonal prediction of extreme weather. The rest of this paper is structured as follows. Section 2 introduces the data, diagnostic analysis methods, and designs of atmospheric global climate model (AGCM) experiments. Section 3 exhibits characteristics of MJO initiation and propagation under the different background IOBM phases and explores mechanisms behind. Section 4 gives summary and discussions for the finding of this study.

2 Data and Methods

2.1 Data processing

To diagnose the MJO-scale convection and circulation and analyze the column-integrated moisture budget during the extended boreal summer (from May to August; MJJA) of 1981–2020 (40 years), we use the daily outgoing longwave radiation (OLR) data from the National Oceanic and Atmospheric Administration (NOAA) (Liebmann & Smith, 1996), the horizontal and vertical winds (u, v, and ω) from NCEP/DOE Reanalysis II (Kalnay et al., 1996; Kanamitsu et al.,

2002) and specific humidity (q) from NCEP/NCAR Reanalysis I (NCEP/NCAR R1 is calculated in postprocessing but NCEP did not do this for R2). The climatological mean, linear trend and annual cycle based on the 1991–2020 reference period are first removed to obtain the daily anomalies, and then a 181-point Lanczos bandpass filter is applied to isolate the intraseasonal (20–90 days) timescale variability associated with MJO. The global monthly SST is from the NOAA Optimum Interpolation SST version 2 (OISSTv2) High Resolution dataset, with a 0.25° squared horizontal resolution (Reynolds et al., 2007). The Niño-3.4 and IOBM indices are respectively defined as the tropical Pacific-averaged (5°S–5°N, 120°–170°W) and tropical Indian Ocean-averaged (20°S–20°N, 40°–100°E) SST anomaly. The Oceanic Niño index (ONI), one measure of the ENSO, is further calculated by the monthly Niño-3.4 index.

The RMM and OLR-based MJO indices (OMI) are used to characterize the trajectory and amplitude of the MJO. The former indices are the leading two principal components (PCs) derived by projecting the equatorially (15°S–15°N) averaged OLR and zonal wind anomalies at 850 hPa (U850 hereafter) and 200 hPa (U200 hereafter) onto the two eigenmodes extracted by Wheeler and Hendon (2004). The OMI is the projection of 20–96-day filtered OLR anomalies, including all eastward and westward wave numbers, onto two eigenmodes of 30–96-day filtered OLR anomalies (Kiladis et al., 2014). The strong MJO days are defined as those when the index amplitude exceeds one standard deviation.

2.2 Methods

This study focuses on changes in MJO activity in response to the interannual IOBM signal without the interference effects of ENSO. Thus, the IOBM months are first selected as those when the IOBM index exceeds the threshold of one standard deviation during the extended

boreal summer. Among the selected months, we excluded the ENSO months defined as those with ONI value exceeding ±0.5 ℃.

An empirical orthogonal function (EOF) analysis method is used here to extract the dominant propagation patterns of intraseasonal convection anomalies under different IOBM conditions. We consider a domain of 40°E to 150°E in the zonal direction, and a wider meridional range of 15°S to 40°N to sufficiently cover the northward shift convection during boreal summer. The regression analysis method is further used to explore how and why MJO characteristics differ in different phases of IOBM. Specifically, the reference time series is defined as the first PC derived above. The intraseasonal-scale variables and moisture budget terms are regressed against the reference time series in following sections.

For the composite analysis, we select MJO episodes when the intraseasonal OLR anomaly averaged over the equatorial Indian Ocean (10°S–10°N, 75°E–95°E) is below -0.5 standard deviation for five consecutive days. The reference date for a selected MJO episode is defined as “Day 0” when the above equatorial Indian Ocean-averaged OLR anomaly reaches its minimum. A total of 134 MJO episodes meeting the aforementioned criteria are preliminarily identified during the 40-year MJJA period, and then twenty-two episodes among them are ultimately available for this study in disregard of IOBM years significantly influenced by ENSO, including respectively eight and fourteen episodes during warm and cold IOBM phases.

Furthermore, the *k*-means clustering analysis is used to objectively classify the selected MJO episodes according to their day-longitude propagation diagrams of OLR anomalies averaged between 10°S and 10°N. The domain used for clustering analysis covers a 30-day period from Days -10 to 20 and a longitudinal extent from 40°E to 180°E. The iterative

algorithm seeks to find an optimal partition of the samples into *k* clusters. The members within each cluster should resemble each other while being efficiently separated from members of other clusters. Michelangeli et al. (1995) provide detailed description of the *k*-means clustering algorithm. Based on the criterion that the number of cluster depends on the mean silhouette value, we choose three as the optimal *k* value.

2.3 Model and experimental design

The model used in this study is adapted from the Community Atmospheric Model version 6.0 (hereafter CAM6) as the atmospheric component of the NCAR Community Earth System Model (CESM) version 2.1 (Danabasoglu et al., 2020). This is the newest version of the CESM with the goal of eventually providing seamless Earth system prediction from weeks to decades. CAM6 is the default atmospherics model with the highest skill in the simulation of the monsoon intraseasonal oscillation compared to other generations (Kumar et al., 2023). It uses a nominal 1° horizontal resolution of 1.9°×2.5° and has 32 vertical levels from the Earth surface to the top of the model lid (~3.6 hPa). Two full AGCM numerical sensitivity experiments are conducted to investigate the impact of the internal IOBM on the MJO during the boreal summer of MJJA, including the warming IOBM run and cooling IOBM run (Exp-WI and Exp-CI in short). They are the forced runs in which the SSTs are specified. In the Exp-WI, the positive SST anomalies in the tropical Indian Ocean (30°S–15°N, 45°E–105°E) during the warm IOBM phase are added into the SST forcing the CAM6, and monthly climatological SST is used in other oceanic areas. The Exp-CI is similar to the Exp-WI, except for the inclusion of cooling SST perturbations during the cold IOBM phase. For each experiment, the model is integrated forward for 20 years and the simulation from the last 15 years are compared with the observational results, with consideration of a 5-year spin-up period.

3 Results

3.1 IOBM phase-dependent features of the MJO during MJJA

We first examine intensity of the MJO by referring to the intraseasonal variance of convection (e.g., OLR) and circulation (e.g., U850) over the Indo-Pacific warm pool. Figures 2a–2b demonstrate that MJO-scale convective signals are strong over the equatorial Indian Ocean, Bay of Bengal (BoB), Arabian Sea, South China Sea (SCS), and western Pacific, consistent with the observational results of Wei et al. (2024). Considerable MJO circulation signals are also observed over these regions and are especially strong over the SCS and the Philippine Sea (Figs. 2d–2e). However, the patterns of MJO variance are distinct between the warm and cold IOBM phases. In terms of convection, the MJO over the western Indian Ocean during the warm IOBM phase is stronger than that during the cold phase (Fig. 2c). In contrast, over the northwestern Pacific and the northern Maritime Continent (MC), the MJO is usually weakened when the Indian Ocean varies from cool to warm phases. In terms of circulation, the IOBM tends to influence the MJO mainly over the South China Sea and Philippine Sea where 850-hPa zonal wind anomalies show smaller intraseasonal variation under the warm IOBM condition (Fig. 2f). Consequently, it can be inferred that the convective activity of the MJO predominantly exhibits a zonal-dipole variation between the Indian Ocean and western Pacific under modulation of IOBM. Recently, it has been indicated that the MJO signal over the Indian Ocean owes its existence to its eastward component during boreal summer (Wei et al., 2024). Therefore, we speculate that the IOBM may saliently influence the initiation and zonal propagation of the boreal summer MJO.

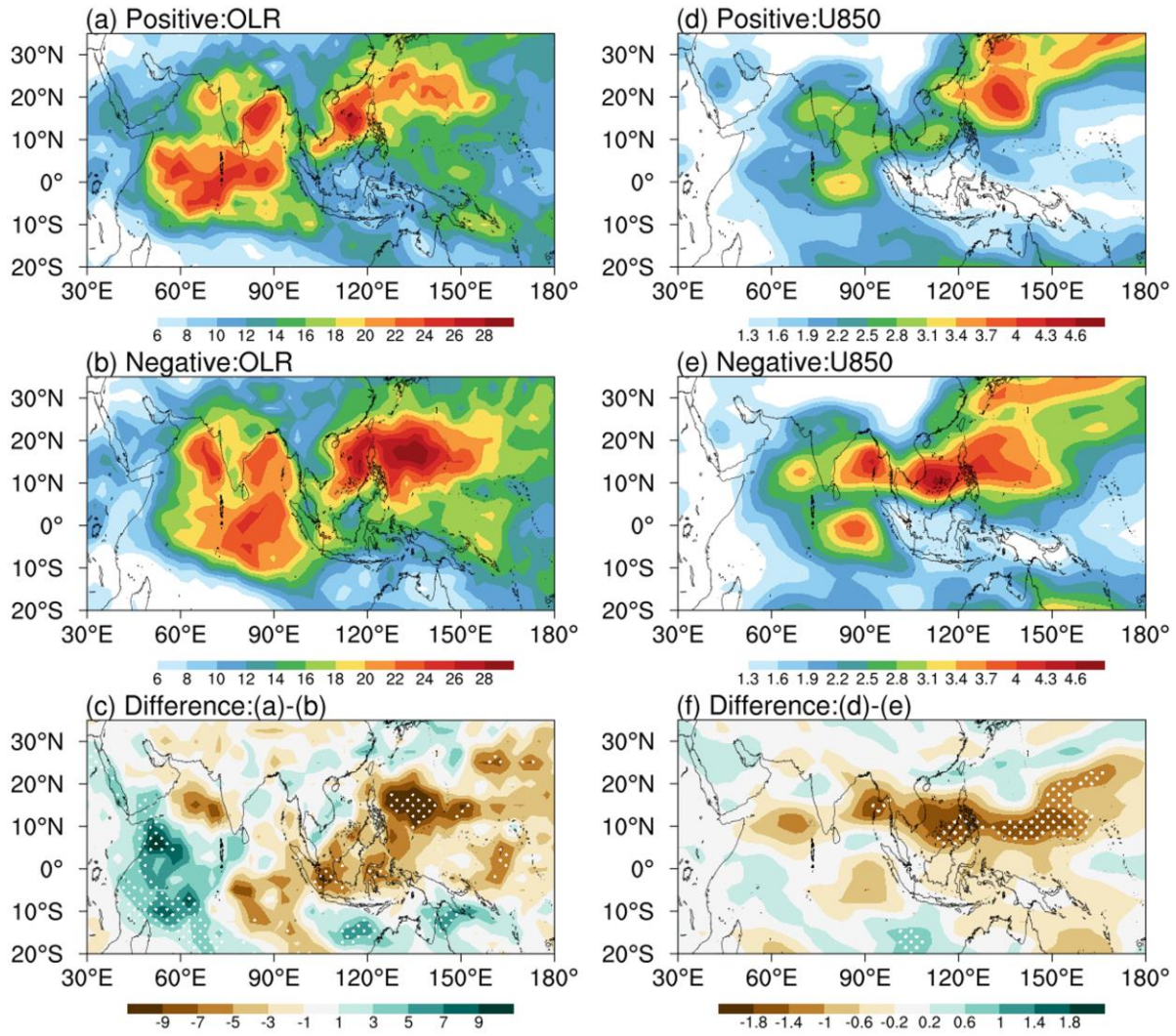

Figure 2. Standard deviation of intraseasonal (left) outgoing longwave radiation (OLR) anomalies and (right) 850-hPa zonal wind (U850) anomalies for the positive (a, d) and negative (b, e) IOBM phases during the extended boreal summer (May–August; MJJA) of 1981–2020. (c, f) The warm subtracts cold IOBM phases. The white stipple denotes the significant difference passing the 90% confidence level based on the parametric *F*-test.

Figures 3a–3d show the index evolution of MJO episodes under the two IOBM phases from Day -15 to Day 25. To examine possible differences of the MJO initiation between the warm and cold IOBM phases, we first construct an index to identify the timing of individual MJO episodes when transiting from positive to negative. In view of the disparity in the latitude range for filtered OLR subjected to an EOF analysis between the OMI and RMM index during

boreal summer, this index is defined as the 20–90-day filtered OLR anomaly averaged in (5°S–15°N, 40°E–120°E). The timing of MJO under the warm IOBM phase is identified at Day -5, when intensity of the MJO episode undergoes a sharply increasing transition, and such a transition is obviously lagged at Day -2 under the cold IOBM phase. Based on these identifications, most MJO episodes under the warm IOBM phase initiate from Phases 1–2 (i.e., the east coastal Africa and the western Indian Ocean), manifesting as a local oscillation over the tropical Indian Ocean (Figs. 3a and 3c), while the initiation of MJO episodes under the cold IOBM phase is located further east over the central Indian Ocean (Phases 2–3; Figs. 3b and 3d).

Figures 3e–3f further compare the occurrence frequency and amplitude of strong MJO days in individual MJO phases between the warm and cold IOBM conditions. The occurrence probability of strong MJOs days in terms of OMI results is more uniformly distributed during the cold IOBM, while during the warm IOBM, active MJOs operate most frequently only in Phase 2 over the western Indian Ocean (Fig. 3e). Similarly in terms of RMM results, the proportion of strong MJO days is significantly higher in Phases 1–4 than in Phases 5–8 during the warm IOBM, but this higher ratio tends to occur in the western Pacific during the cold IOBM (Fig. 3f), which supports the conjecture from the standard deviation fields (Fig. 2). Thus, the IOBM signal has a significant regional effect on the formation of MJO convection, particularly on its initiation, as previously reported in literature (e.g., Wu et al., 2023).

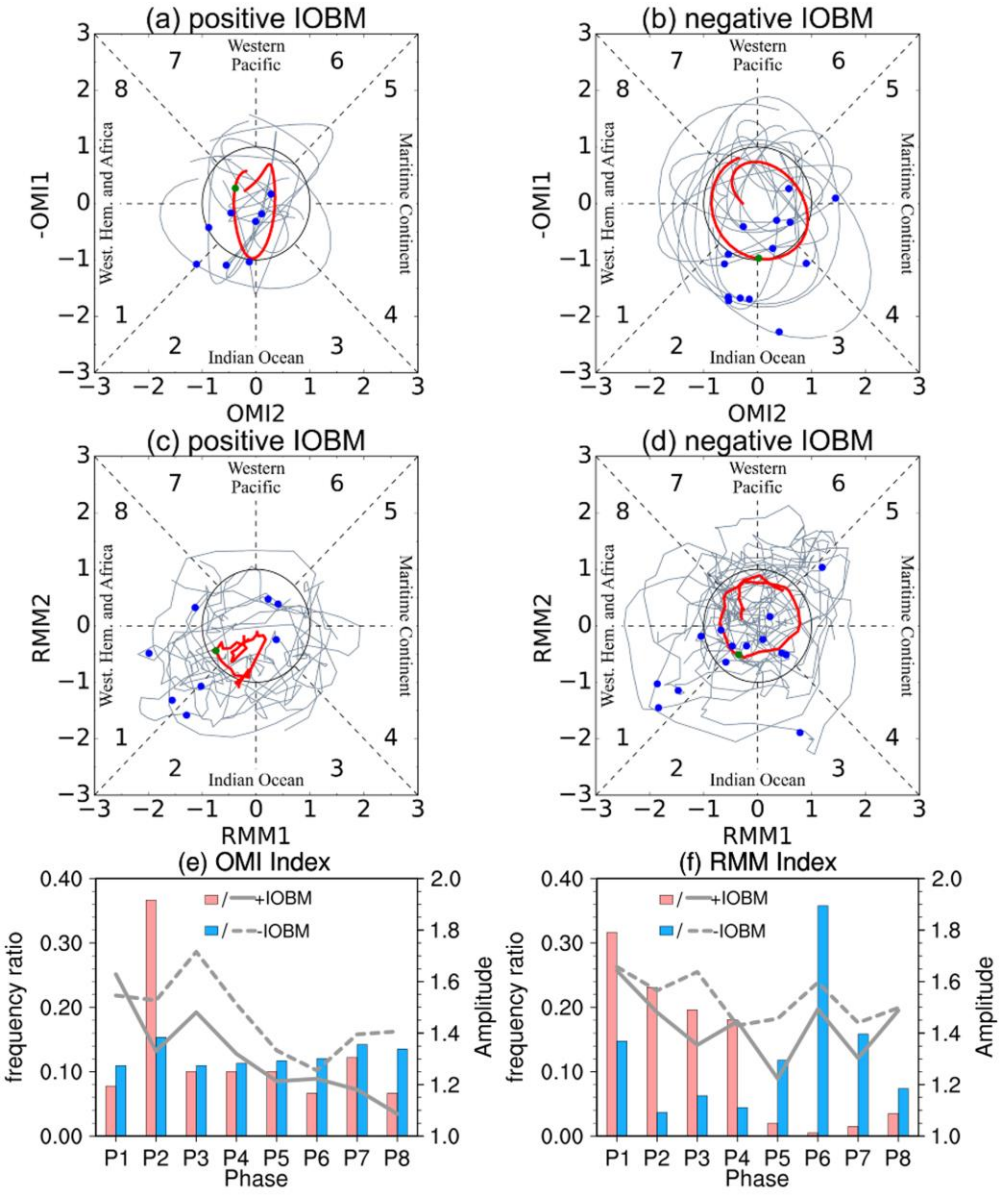

Figure 3. MJO-related statistics under the positive (a, c) and negative (b, d) IOBM conditions during MJJA of 1981–2020. The OLR-based MJO index (OMI; a–b) and RMM index (c–d) of MJO episodes track from Day -15 to Day 25. Gray lines show individual MJO cases (Day -5 (a, c) and Day -2 (b, d) as blue dots). The red line showcases the composite for all cases, and the green dot represents the composite of blue dots. (e) Occurrence frequency (bar) and composite amplitudes (line) of OMI index in Phases 1–8 under the positive (red bar and solid line) and negative (blue bar and dashed line) IOBM. The index is selected when its amplitude exceeds 1.0. (f) is the same as (e), but for the RMM index.

To investigate how MJO propagates under different IOBM phases, we extract the first two EOF modes of 20–90-day filtered OLR anomalies over (15°S–40°N, 40°E–150°E) during

boreal summer (Fig. 4). Under the warm IOBM: the first EOF pattern shows a meridional dipole, with negative loading in the equatorial Indian Ocean and positive one over the Arabian Sea-Bay of Bengal-SCS (Fig. 4a); the second EOF shows a zonally elongated convection pattern, spanning from Indian Ocean to SCS and centered at ~10°N (Fig. 4b). Thus, the background warming of entire Indian Ocean may not support an MJO propagates smoothly across the MC and into western Pacific. Instead, the intraseasonal convection might behave as northward-only propagation confined over the Indian Ocean. However, when the entire Indian Ocean is cooled, there appear evident convection anomalies over the western Pacific in both EOFs (Figs. 4c–4d). Besides, the second EOF manifests a canonically northwest-southeast tilt structure of the deep convection (Fig. 4d). The cross-correlation analysis suggests that EOF1 virtually leads EOF2 by ~10 days. Thus, not only the northward propagation, but also the eastward propagation is a major feature of the intraseasonal convection under the cold IOBM phase, as is typical for the boreal summer MJO (Kikuchi, 2021).

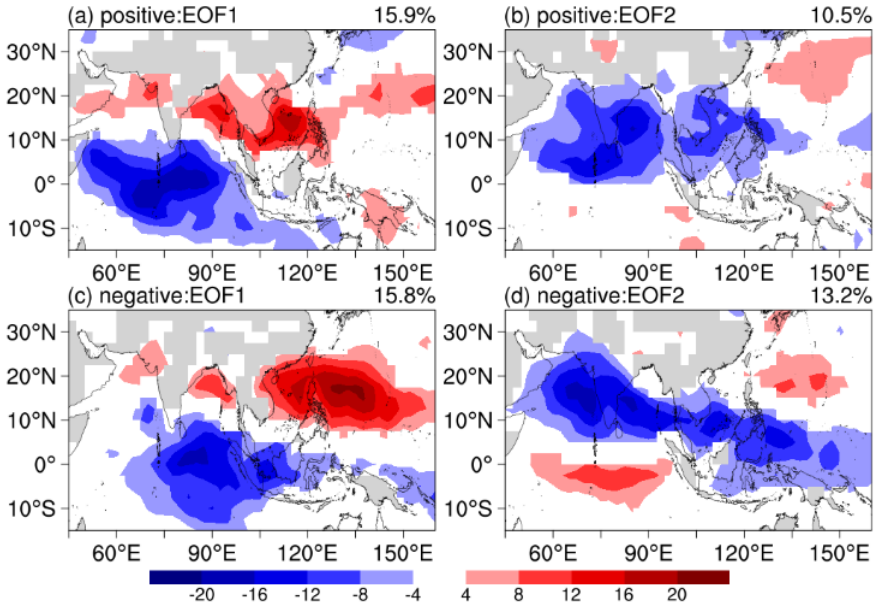

Figure 4. (a) Spatial patterns of the first two leading empirical orthogonal functions (EOFs) of daily intraseasonal OLR anomalies under the positive (a, b) and negative (c, d) IOBM during

MJJA of 1981–2020. The explained variances are indicated in the top right corner of each panel.

Given the leading EOF patterns, Figure 5 further illustrates the corresponding propagation characteristics through their associated intraseasonal convection and circulation. Additionally, composite diagrams of MJO episodes are employed to verify if similar features can be observed for the MJO propagation. We can clearly see that the zonal propagation of MJO from the tropical Indian Ocean into western Pacific exhibits pronounced differences between the two phases of IOBM. Under the cold IOBM (Figs. 5b), there is a leading suppressed convection (i.e., positive OLR anomalies) over the MC between lag days -15 and -2 when the enhanced convection initiates over the central Indian Ocean (~85°E). The MJO propagates eastward at a speed of ~5.0 m/s following the method of Wei & Ren (2019), and after reaching the MC, the convective signals weaken somewhat but re-develop over the western Pacific (Fig. 5b); whereas under the warm IOBM, the MJO initiates further west over the western Indian Ocean (~60°E), and the suppressed convection is much less organized (Figs. 5a). During its traveling across the Indian Ocean, the MJO propagates towards the MC at a slower speed of 4.5 m/s, and then weakens sharply and decays rapidly (Fig. 5a). Compared to the cold IOBM, similar results can be seen in Figs. 3e–3f under the warm IOBM, where the amplitudes of both the OMI and RMM indices generally decrease more rapidly with phase, and the frequency ratio of RMM Phases 5-8 is apparently lower. We also examine the northward propagation of MJO over the equatorial Indian Ocean (Figs. 5c–5d) and find that the more robust MJO convection-circulation coupled anomalies, can propagate to ~20°N during the cold IOBM compared to only 12°N during the warm IOBM.

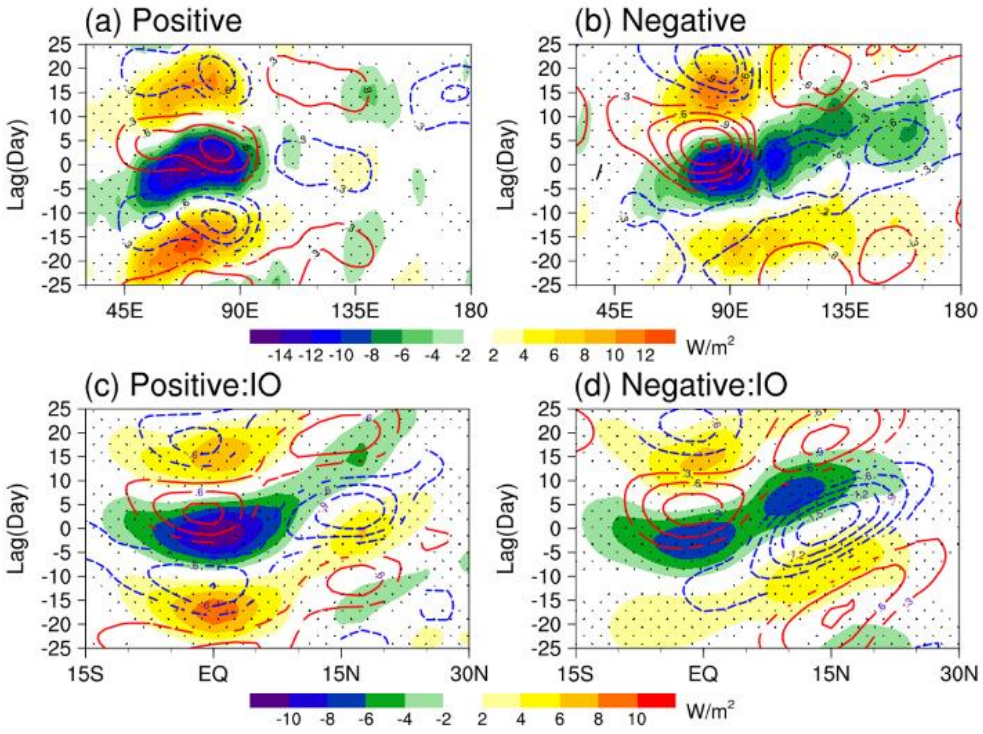

Figure 5. Lead-lag regressions of the intraseasonal OLR (shading; units: W/m^2) and U850 anomalies (contour; units: m/s) averaged over the equatorial zone (5°S–5°N; a–b) and the Indian Ocean zone (40°E–100°E; c–d) onto the PC1 index for the positive (a, c) and negative (b, d) IOBM phases during MJJA of 1981–2020. The red solid contour indicates positive value, and the negative one for the blue dash contour. The stipple denotes those OLR anomalies above the 90% confidence level, and the U850 anomalies at the same confidence level are only shown.

After having demonstrated the IOBM impacts on the MJO propagation, to better understand the IOBM-dependent zonal propagation patterns of MJO during boreal summer, we subdivide these MJO episodes by clustering analysis (Fig. 6). It reveals notable distinctions among the three clusters: Cluster #1, accounting for 27.3% of all MJO episodes, exhibits comparable propagation behaviors to the MJO under the warm IOBM (Fig. 6a). The deep convection of Cluster #1 initiates from the western Indian Ocean (~60°E) and propagates slowly towards the eastern Indian Ocean (~115°E), but then rapidly weakens due to the lack of suppressed conditions ahead; Cluster #2, accounting for 40.9% of all, exhibits a westward-propagating pattern in the western Pacific where the convective signals merge with deep

299 convection from the Indian Ocean (Fig. 6b); Cluster #3, accounting for 31.8% of all, behaves
300 more like the MJO under the cold IOBM (Fig. 6c). The enhanced convection of Cluster #3
301 originates from the central Indian Ocean (~90°E) and proceeds with the stronger eastward-
302 propagating mode to the western Pacific. Besides, we further compare the statistical quantity
303 proportion of MJO episodes in each cluster between the two IOBM phases (Table. 1). In the
304 observations, Cluster#1 accounts for the largest proportion (37.5%) among the three clusters
305 under the warm IOBM, while Cluster#3 (35.71%) has a much higher proportion than Cluster#1
306 (21.43%) under the cold IOBM. It again proves that the MJO influenced by the warm IOBM
307 tends to propagate like Cluster#1, and the dominant propagation of the cold IOBM-influenced
308 MJO is more like Cluster#3.

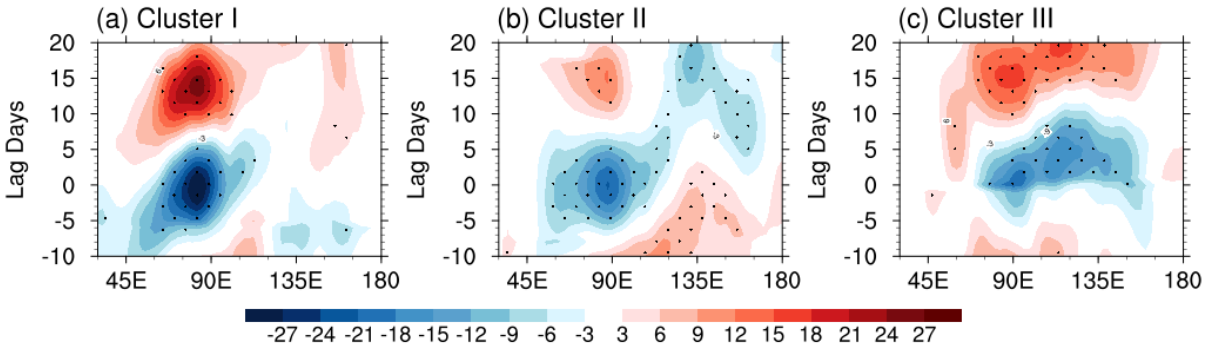

309

310 **Figure 6.** Three clusters of composited lag-longitude diagram of intraseasonal OLR anomalies
311 (units: W/m^2) between 5°S and 5°N by the *k*-means cluster analysis under both the positive and
312 negative IOBM phases during MJJA of 1981–2020. The stipple denotes those OLR anomalies
313 above the 95% confidence level.
314

Table 1. The result of *k*-means cluster analysis on the observation and model values of MJO cases under the two IOBM phases from May to August

Order of Cluster	Positive IOBM		Negative IOBM	
	Observation	Model	Observation	Model
I	37.5%	40.0%	21.43%	21.95%
II	37.5%	27.5%	42.86%	36.58%
III	25.0%*	32.5%*	35.71%*	41.46%*

*: the percentage of MJO cases with a clear eastward-propagating characteristic

315

3.2 Mechanisms of MJO variation with IOBM phase

We further reveal causes of the different MJO features between the two IOBM phases. In the warm IOBM, a notable feature is the larger area of warm ocean (i.e., >29°C) extending westward into the Indian Ocean compared to the cold IOBM (Figs. 7a–7b). This suggests that the westward shift of MJO initiation is associated with the westward expansion of warm ocean. An anomalous low-level anticyclonic circulation appears over the northwestern Pacific, and locally easterly shear anomalies are observed over the west coast of South Africa (Figs. 7c and 7e). Stronger easterly shear can enhance the coupling of baroclinic and barotropic modes of the Rossby waves. Since the barotropic component is a modified Rossby mode and only excited by Rossby waves, the easterly shear can efficiently transform from baroclinic energy to barotropic energy, enhancing barotropic vorticity and thus low-level Rossby waves (Wang & Xie, 1996, 1997). In addition, stronger vertical shear in the warm IOBM, regardless of its sign (i.e. westerly or easterly shear), tends to slow down the westward propagation of Rossby waves (Wang & Xie, 1996). In the cold IOBM (Figs. 7d and 7f), the low-level anomaly circulation over the northwestern Pacific conversely becomes cyclonic, and associated weaker easterly shear over the entire Indian Ocean is conducive to the growth of eastward-propagating tropical waves (e.g., Khouider & Majda, 2008; Majda & Stechmann, 2009; Lu & Hsu, 2017). Accordingly, the combined effect of the stronger Rossby wave and weaker Kelvin wave components during the warm IOBM results in a slower MJO propagation.

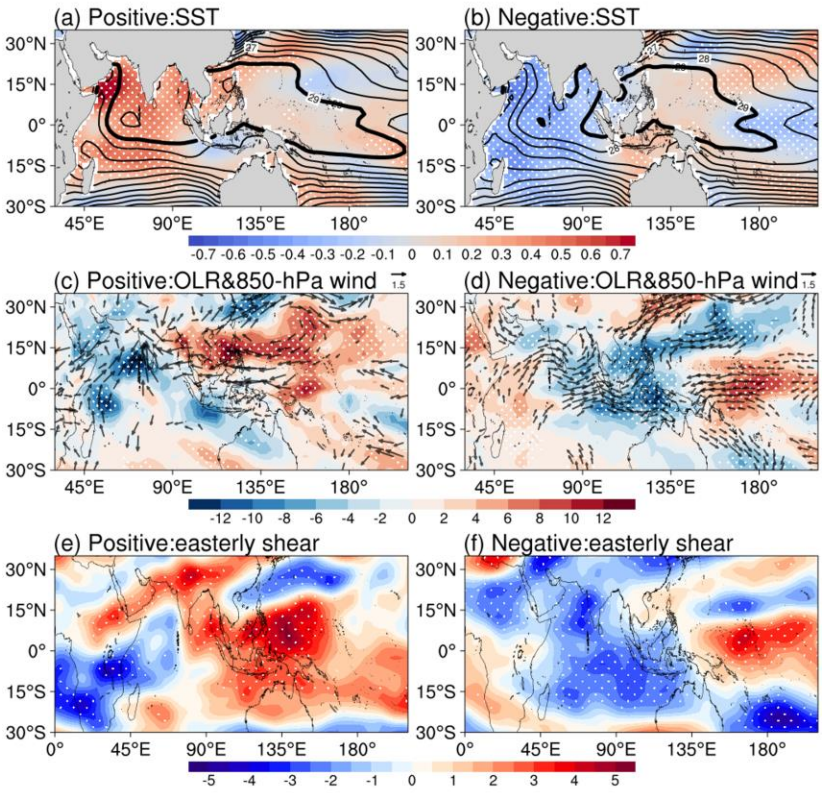

Figure 7. Background states under the positive (left) and negative (right) IOBM phases. (a–b) show the anomalous (shading, units: ℃) and total (contours with an interval of 1 ℃) background sea surface temperature; (c–d) show the background OLR anomalies (shading, units: W/m^2) and 850-hPa wind anomalies (vectors with a reference of 1.5 m/s); (e–f) show the associated anomalous vertical shear of background zonal wind (defined as U200-U850, units: m/s). The stipple denotes those above the 90% confidence level.

To further understand potential structural differences of MJO between the two IOBM phases, Figure 8 shows the vertical structures of the MJO-related anomalous circulation and moisture and its tendency at Day 0. We can see that a deeper and better organized front Walker Cell (FWC; Chen & Wang, 2018) coupled with moisture appears to the east of the enhanced convection center over the Indian Ocean (105°E–165°E) under the cold IOBM (Fig. 8b). This FWC is primarily initiated by the leading suppressed convection, manifesting as a strong easterly anomaly in the planetary boundary layer (PBL) and lower troposphere (Fig. 8f). Previous studies have indicated that FWC could strengthen Kelvin wave easterly anomalies and cause a pre-

moistening and heating perturbation ahead of MJO deep convection (e.g., Wei & Ren, 2019, 2022). The stronger lower-level moistening below 500 hPa under the cold IOBM is matched with the ascending motions caused by the FWC-related Kelvin wave PBL convergence (Figs. 8c–8d). The ascending motion could destabilize the lower-level atmosphere through vertical moisture transport, which plays a prominent role in the development of shallow and congestus convection (Wang et al., 2017; Wei & Pu, 2021). In contrast, under the warm IOBM, there exists no significant zonal FWC wind anomaly ahead of MJO deep convection, corresponding well to the slow MJO propagation (Fig. 8e).

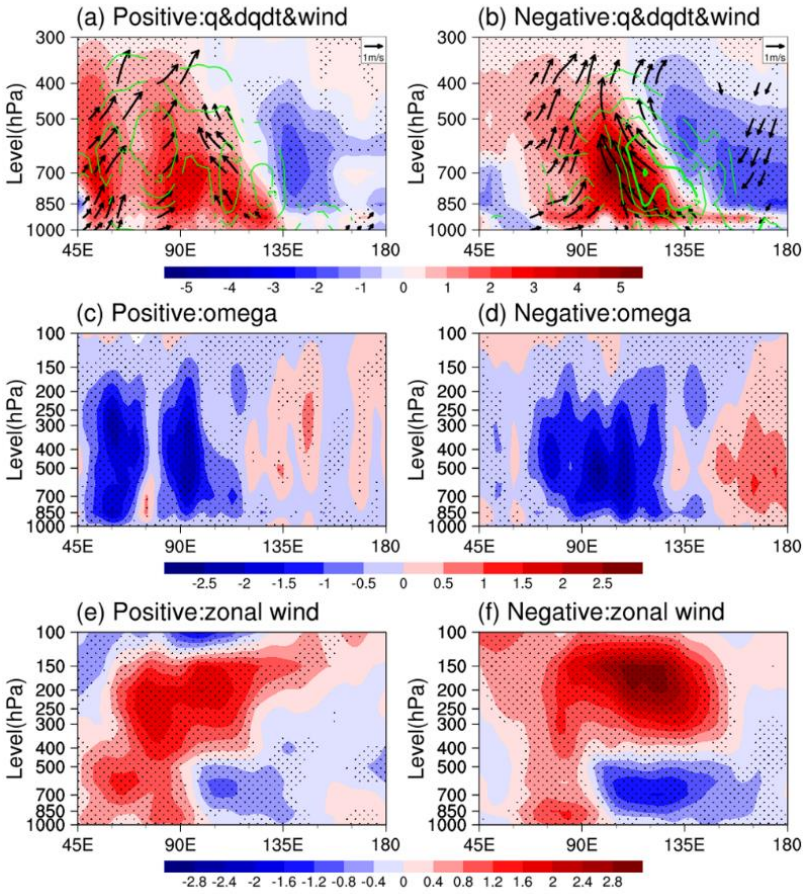

Figure 8. Vertical structures of the equatorial (5°S–5°N) intraseasonal specific humidity anomalies (a–b; shading; units: $\times 10^{-1}$g/kg) and their temporal tendency anomalies (a–b; contour; units: $\times 10^{-1}$ g/(kg·day)), (u, $\omega \times 100$) anomalies (a–b; vector), vertical velocity anomalies (ω) (c–d; units: $\times 10^{-2}$ Pa/s) and zonal wind anomalies (u) (e–f; units: m/s) regressed onto the PC1 index at

Day 0 for the positive (a, c, e) and negative (b, d, f) IOBM phase during MJJA of 1981–2020. The stipple denotes those statistically significant above the 95% confidence level. The vectors and contours in (a) also only show values above the same confidence level.

Besides, the vertical structure of moisture tendency is displayed in Fig. 8a–8b. The significantly positive moisture tendency under the cold-IOBM phase is found in front of the MJO convection and extends to the western Pacific (~155°E) below 500 hPa (Fig. 8b), whereas weaker positive moisture tendency with weaker vertical tilting exists to the east under the warm IOBM (Fig. 8a). It can cause a zonally asymmetric accumulation of moisture, as indicated by the "moisture mode" theory (Adames & Kim, 2016), favoring the eastward propagation of MJO. Meanwhile, the positive moisture anomalies might result from the large-scale advective processes (Kim et al., 2014; Wei & Ren, 2019). To comprehend which physical processes produce positive moisture tendency, we here conduct the moisture budget analysis, which has been widely employed to understand the moistening process during the MJO propagation across the Indian Ocean (e.g., Adames & Kim, 2016; Ren et al., 2021; Wei & Ren, 2022). The intraseasonal column-integrated budget equation at a constant pressure level can be written as follows (Yanai et al., 1973):

$$\left\langle \frac{\partial q}{\partial t} \right\rangle' = -\left\langle u \frac{\partial q}{\partial t} \right\rangle' - \left\langle v \frac{\partial q}{\partial y} \right\rangle' - \left\langle \omega \frac{\partial q}{\partial p} \right\rangle' - \left\langle \frac{Q_2}{L_v} \right\rangle', \quad (1)$$

where Q_2 and L_v are the apparent moisture sink and the evaporation coefficient of latent heating, respectively, $\langle\ \rangle$ denotes the column integration from surface to 500hPa, and the prime symbol does the 20–90-day bandpass filtering to obtain the MJO-scale anomalies. The first three terms on the right-hand side of Eq. (1) are the zonal (*uHadv*), meridional (*vHadv*), and vertical moisture advection. The fourth term is the net moistening effect of microphysical and eddy

diffusion processes (Hsu & Li, 2012; Chen et al., 2016), considered as the difference between the local moisture tendency and the moisture advection (Wei & Ren, 2022). The sum of last two terms can be called "*Column process*", representing the large-scale vertical moisture advection, microphysical processes and vertical eddy moisture fluxes (Chikira, 2014; Wei & Pu, 2021).

The tropospheric advection processes are explored over the western Pacific (5°S–15°N, 130°E–155°E), the region associated with zonal asymmetry of moisture tendency. The individual terms of Eq. (1) regressed onto the PC1 at Day 0 are shown in Fig. 9. The MJO moisture tendency is stronger under the cold IOBM phase than the warm phase, which is mainly attributed to the difference of *vHadv* (Fig. 9a), as the previous results (Kim et al., 2014; Pillai & Sahai, 2016; Wei & Ren, 2019). To further examine relative roles of the eddy-eddy and eddy-mean flow interactions, variations in the meridional velocity and specific humidity can be divided into three time scales, as follows (Hsu & Li, 2012; Wang et al., 2017):

$$\begin{aligned} q &= q_L + q_M + q_H, \\ v &= v_L + v_M + v_H, \end{aligned} \quad (2)$$

where x_L, x_M, and x_H denote anomalies of the low-frequency (i.e., $>$90 days) background state, 20–90-day intraseasonal, and high-frequency (i.e., $<$20 days) components, respectively. Therefore, further investigation on the decomposition of *vHadv* is performed as follows:

$$vHav = \underbrace{-(v_L \frac{\partial q_L}{\partial y})'}_{\text{T1}} \underbrace{-(v_L \frac{\partial q_M}{\partial y})'}_{\text{T2}} \underbrace{-(v_L \frac{\partial q_H}{\partial y})'}_{\text{T3}} \underbrace{-(v_M \frac{\partial q_L}{\partial y})'}_{\text{T4}} \underbrace{-(v_M \frac{\partial q_M}{\partial y})'}_{\text{T5}} \underbrace{-(v_M \frac{\partial q_H}{\partial y})'}_{\text{T6}} \underbrace{-(v_H \frac{\partial q_L}{\partial y})'}_{\text{T7}} \underbrace{-(v_H \frac{\partial q_M}{\partial y})'}_{\text{T8}} \underbrace{-(v_H \frac{\partial q_H}{\partial y})'}_{\text{T9}} \quad (3)$$

where the nine terms in Eq. (3) are simplified as Tn (n=1, …, 9) from left to right. Figure 9b displays the meridional moisture advection terms of Eq. (3) at Day 0 in the warm and cold phases of IOBM, respectively. The moistening is mainly attributed to three terms: advection of

MJO moisture by the low-frequency background meridional flow (T2), advection of background moisture by the MJO flow (T4), and advection of high-frequency moisture by the high-frequency flow (T9). Among them, the eddy moistening effect T9 contributes the most of meridional advection processes, which is consistent with the conclusion of Wei et al. (2022).

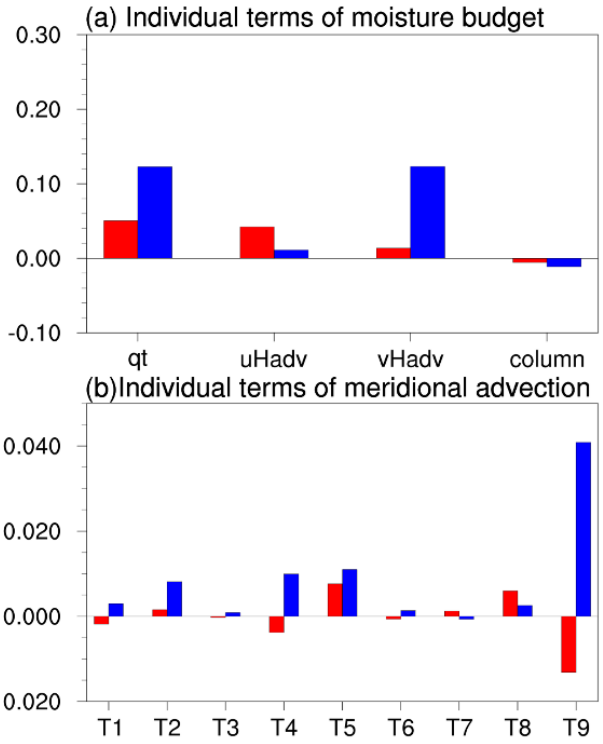

Figure 9. Column-integrated (1000–500 hPa) moisture budget for MJO at Day 0 during positive (red bar) and negative (blue bar) IOBM phases. (a) The individual terms of Eq. (1) averaged over (5°S–15°N, 130°E–155°E) regressed onto the PC1 index, including the moisture tendency (*qt*; units: kg/(m^2·day)), zonal horizontal advection (*uHadv*; units: kg/(m^2·day)), meridional horizontal advection (*vHadv*; units: kg/(m^2·day)), and net contribution of column processes (*column*; units: kg/(m^2·day)). (b) As in (a), but for the individual terms of moisture meridional advection (units: kg/(m^2·day)).

3.3 AGCM sensitivity experiment

Two sets of AGCM experiments are conducted to validate the above observational results (see details of experiments in Section 2.3). Figure 10 presents the simulated MJO-scale variance during MJJA under both warm and cold IOBM phases. Despite minor discrepancies in overall

values between the simulations and observations, our conclusion that they bear a resemblance to each other remains valid (Fig. 2). The major differences in MJO convection and circulation centers between the two IOBM phases are basically consistent with observations (Figs. 10c and 10f), although the sensitivity experiment slightly underestimates convection over the eastern Indian Ocean and overestimates convection to the east of 145°E. For example, the stronger MJO convection over the western Indian Ocean under the warm IOBM is well reproduced in the experiment, as compared to cold IOBM conditions (Fig. 10c). The relatively weaker variance of U850 anomalies over the SCS is also captured in Exp-WI (Figs. 10d and 10f). Consequently, this effectively underscores the pivotal role of independent variations in SST pattern within the tropical Indian Ocean in driving changes in the MJO intensity.

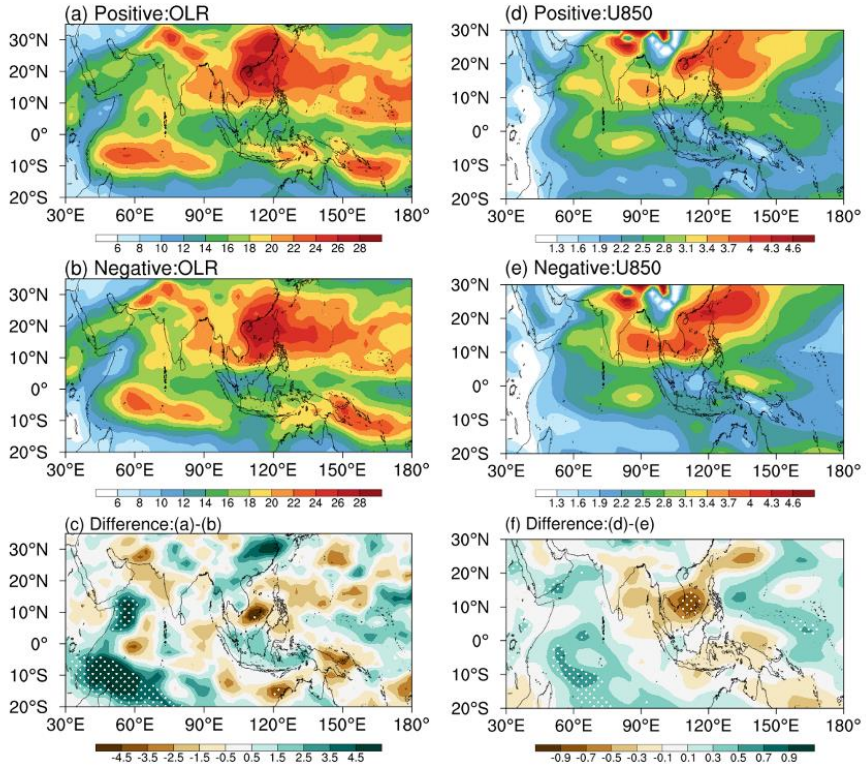

Figure 10. Same as Figure 2, but for the model simulation.

Following the observational diagnosis methods (Figs. 5a–5b), the intraseasonal simulated OLR and U850 anomalies are regressed onto the MJO index defined by the normalized intraseasonal simulated OLR averaged in the tropical Indian Ocean (15°S–15°N, 40°E–120°E). The MJO convective activity in Exp-WI is confined to the western Indian Ocean with an extremely slow propagation (Fig. 11a), whereas the Exp-CI experiment shows a clearer eastward propagation. Moreover, the initiation of MJO convection in Exp-CI exhibits a more easterly displacement (Fig. 11b). Although the deep convection in Exp-CI coupled with circulation has some limited propagation through the MC, it is still able to reach the western Pacific, and the associated intraseasonal low-level easterly is also much stronger than that in Exp-WI. Besides, based on the methods of clustering analysis and selecting observational MJO events in Section 2.2, a total of 40 simulated MJO events are identified in Exp-WI, while Exp-CI has 41 such events. These events are subsequently categorized into three distinct clusters. The resulting zonal propagation patterns correspond well with the observations in Figure 6 (not shown). As shown in Table 1, Cluster#1 accounts for the most proportion among all the clusters under the warm IOBM, which covers respect 37.5% and 40% of all MJO episodes in the simulations and observations. While under the cold IOBM, the percentage of Cluster#3 in observation (35.71%) and simulation (41.46%) are both higher than that of Cluster#1 (21.43% and 21.95%, respectively). This provides additional evidence that the MJO of Cluster #1 features a locally slow propagating oscillation, while that of Cluster #3 has a more distinct eastward propagating feature. It confirms the observational result that the change of IOBM phase can modulate the initiation location and eastward propagation of the MJO during the boreal summer.

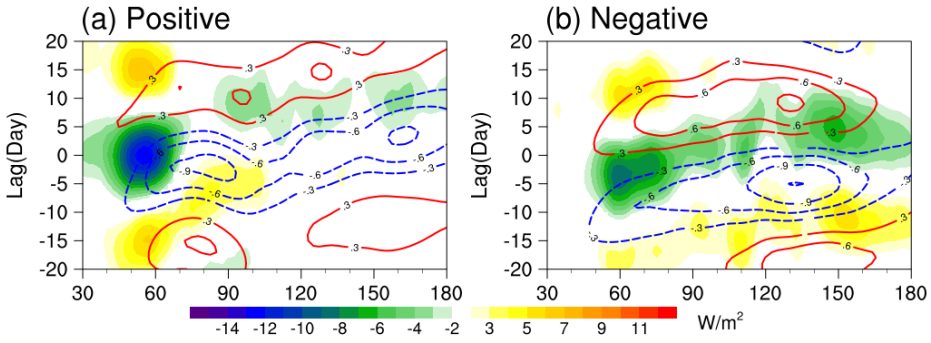

Figure 11. Same as Figures 2a and 2b, but for the regressed anomalies of the model simulation over the Indian Ocean region (15°S–15°N, 40°E–120°E).

4 Summary and discussions

4.1 Concluding Remarks

As a dominant mode of tropical intraseasonal variability, the MJO significantly influences global weather and climate. Previous studies have mainly attributed the interannual variations in MJO initiation and propagation to the modulation effects of ENSO (e.g., Klein et al., 1999; Yang et al., 2007). However, whether the Indian Ocean warming independent of ENSO modulates the MJO is seldom examined. To address this gap, we conducted a comprehensive analysis using observational datasets and model experiments to explore the differences in MJO initiation and propagation between warm and cold phases of the IOBM independent of ENSO during the boreal extended summer of MJJA.

Our analysis has revealed distinct regional variations in the intensity of MJO variability. Compared to the cold IOBM phase, the warm phase exhibits a pronounced amplification of MJO circulation and convection over the western side of the MC, while concurrently a reduction over its eastern counterpart. Both OMI and RMM trajectories of MJO episodes also indicate a local oscillation over the Indian Ocean, with more frequent occurrence of Phases 1-2. In contrast,

under the cold IOBM phase, MJO convective activity typically starts from Phases 2-3 (i.e., over the central Indian Ocean). The frequency of strong MJO days is significantly higher in Phases 1-4 than in Phases 5-8 of the RMM index during the warm IOBM phase, suggesting that most MJO activity occurs within the Indian Ocean. Furthermore, IOBM strongly influences MJO propagation: under the warm IOBM phase, MJO eastward propagation across the Indian Ocean is relatively slower and quickly dampens upon encountering MC, resulting in a locally standing oscillation. Conversely, the MJO under the cold IOBM phase can smoothly propagate across the MC and even re-develop over the western Pacific, minicking a canonical propagation pattern (Jiang et al., 2020). The *k*-means cluster analysis further indicates similar zonal propagation modes for warm and cold IOBM phases observed in Cluster#1 and Cluster#3 respectively.

We aim to understand the mechanisms of MJO feature contrasts under different IOBM phases by first examining background mean states. Compared to the cold IOBM, the warm IOBM is characterized by a westward shift of 29℃ total warm water over the Indian Ocean, resulting in more westward-initiated MJO episodes. Additionally, the warm IOBM induces an anomalous anticyclone circulation over the northwestern Pacific and stronger easterly shears from the west coast of South Africa to the western Indian Ocean, which synergistically triggers a stronger Rossby wave and weaker Kelvin wave component, inhibiting eastward propagation of MJO. Secondly, by diagnosing large-scale dynamical and thermodynamical variables on an intraseasonal time scale, we find that a prominent distinction between warm IOBM-dependent and cold IOBM-dependent MJO episodes lies in the strength of FWC-related Kelvin wave response. Under warm IOBM conditions, suppressed FWC leading MJO deep convection coupled with weaker pre-moistening and heating perturbation results in weaker easterly

anomalies in PBL and lower troposphere. The relevant ascending anomalies are further reduced, causing the slow MJO propagation.

The differences of MJO propagation between the two phases of IOBM in the context of "moisture mode" are mainly attributed to the different vHav process, which aligns with our previous understanding that the vHav process causes eastward propagation of MJO (Adames & Kim, 2016; Wang et al., 2017; Wei & Ren, 2022). A timescale decomposition analysis suggests that during the cold IOBM phase, a stronger vHav process is primarily contributed by eddy moistening effects, namely, advection of high-frequency moisture by high-frequency flow, followed by advection of MJO moisture by low-frequency background meridional flow and the advection of background moisture by the MJO flow. Full AGCM experiment result does validate that the IOBM phase influences the initiation and propagation of the MJO. Despite some model biases, the major differences of simulated MJO convection and circulation between two IOBM phases are basically consistent with observations. For example, the farther MJO propagation under the cold IOBM can be captured by the sensitivity experiments. Besides, like the observations, the model MJO episodes during the IOBM phase can also be classified into three clusters. The propagation patterns of Cluster#1 and Cluster#3 can well correspond to those in observation under the warm and cold IOBM phase, respectively.

4.2 Discussions

In recent decades, significant changes have occurred in the global climate, including the anomalous warming of SST. This study focuses on comparing the mechanisms of the zonal propagation of MJO under the different IOBM phase. One may further use mechanisms refined here to focus on decadal IO warming to fully understand how global warming could affect MJO

features. While the cause of the differences of MJO northward propagation has not yet explained, but we speculate that the distinct background easterly shear is an important factor. Besides, as we only turn our vision into the interannual variability of the IOBM without the influence of ENSO, the number of MJO episodes available for this study is relatively small. Therefore, the next step is to further investigate the conclusions of this study with large sample model simulation dataset. Recently, Cao et al. (2024) have identified a notable westward migration in the annual mean tropical cyclone genesis across the southern Indian Ocean occurred since 1979. We also found that the linear trend of SST resembles the warm IOBM phase. It is also worth further exploring the potential relationship between the interannual variation of the IOBM, MJO initiation and tropical cyclone genesis location.

Acknowledgments

This work is jointly supported by the National Natural Science Foundation of China (Grants 42175052, 42305056, and U2242206). The AGCM experiments were carried out at the National Supercomputer Center in Tianjin, China. The Optimum Interpolation SST version 2 (OISSTv2) High Resolution dataset is provided by the NOAA, Physical Sciences Laboratory (https://psl.noaa.gov/data/gridded/data.noaa.oisst.v2.highres.html). The daily circulation and outgoing longwave radiation (OLR) data are achieved at https://psl.noaa.gov/data/gridded/tables/daily.html. The RMM index is obtained from the Australian Bureau of Meteorology (http://www.bom.gov.au/climate/mjo/), daily OLR-based MJO index (Kiladis et al., 2014) from https://www.psl.noaa.gov/mjo/mjoindex/.

References

Adames, Á. F., & Kim, D. (2016). The MJO as a Dispersive, Convectively Coupled Moisture Wave: Theory and Observations. *Journal of the Atmospheric Sciences*, *73*(3), 913–941. https://doi.org/10.1175/JAS-D-15-0170.1

Adames, Á. F., & Wallace, J. M. (2015). Three-Dimensional Structure and Evolution of the Moisture Field in the MJO. *Journal of the Atmospheric Sciences*, *72*(10), 3733–3754. https://doi.org/10.1175/JAS-D-15-0003.1

Bai, L., Ren, H.-L., Wei, Y., Wang, Y., & Chen, B (2023). Influence of Madden–Julian Oscillation on Precipitation over the Tibetan Plateau in Boreal Summer. *Atmosphere*, *14*(1), 70. https://doi.org/10.3390/ atmos14010070

Cai, W., Wu, L., Lengaigne, M., Li, T., McGregor, S., Kug, J.-S., et al. (2019). Pantropical climate interactions. *Science*, *363*(6430), eaav4236. https://doi.org/10.1126/science.aav4236

Cao, X., Watanabe, M., Wu, R., Wu, L., Deng, D., Ha., Y., et al. (2024). Westward shift of tropical cyclogenesis over the southern Indian Ocean. Environmental Research Letters, 19(3), 034016. https://doi.org/10.1088/1748-9326/ad1d9b

Chen, G., & Wang, B. (2017). Reexamination of the Wave Activity Envelope Convective Scheme in Theoretical Modeling of MJO. *Journal of Climate*, *30*(3), 1127–1138. https://doi.org/10.1175/JCLI-D-16-0325.1

Chen, G., & Wang, B. (2018). Effects of Enhanced Front Walker Cell on the Eastward Propagation of the MJO. *Journal of Climate*, *31*(19), 7719–7738. https://doi.org/10.1175/JCLI-D-17-0383.1

Chen, X., Ling, J., & Li, C. (2016). Evolution of the Madden–Julian Oscillation in two types of El Niño. *Journal of Climate*, *29*(5), 1919–1934. https://doi.org/10.1175/JCLI-D-15-0486.1

Chikira, M. (2014). Eastward-Propagating Intraseasonal Oscillation Represented by Chikira–Sugiyama Cumulus Parameterization. Part II: Understanding Moisture Variation under Weak Temperature Gradient Balance. *Journal of the Atmospheric Sciences*, *71*(2), 615–639. https://doi.org/10.1175/JAS-D-13-038.1

Danabasoglu, G., Lamarque, J.-F., Bacmeister, J., Bailey, D. A., DuVivier, A. K., Edwards, J., et al. (2020). The Community Earth System Model Version 2 (CESM2). *Journal of Advances in Modeling Earth Systems*, *12*(2), e2019MS001916. https://doi.org/10.1029/2019MS001916

Ding, Y., Liu, Y., & Hu, Z.-Z. (2021). The Record-breaking Mei-yu in 2020 and Associated Atmospheric Circulation and Tropical SST Anomalies. *Advances in Atmospheric Sciences*, *38*(12), 1980–1993. https://doi.org/10.1007/s00376-021-0361-2

Hendon, H. H., Wheeler, M. C., & Zhang, C. (2007). Seasonal dependence of the MJO–ENSO relationship. *Journal of Climate*, *20*(3), 531-543. https://doi.org/10.1175/JCLI4003.1

Hsu, P.-C., & Li, T. (2012). Role of the boundary layer moisture asymmetry in causing the Eastward Propagation of the Madden–Julian Oscillation. *Journal of Climate*, *25*(14), 4914–4931. https://doi.org/10.1175/JCLI-D-11-00310.1

Hsu, P.-C., & Xiao, T. (2017). Differences in the initiation and development of the Madden–Julian oscillation over the Indian Ocean associated with two types of El Niño. *Journal of Climate*, *30*(4), 1397–1415. https://doi.org/10.1175/JCLI-D-16-0336.1

589 Jiang, X., Li, T., & Wang, B. (2004). Structures and Mechanisms of the Northward Propagating
590 Boreal Summer Intraseasonal Oscillation. *Journal of Climate, 17*(5), 1022–1039.
591 https://doi.org/10.1175/1520-0442(2004)017<1022:SAMOTN>2.0.CO;2
592 Jiang, X., Adames, Á. F., Kim, D., Maloney, E. D., Lin, H., Kim, H., et al. (2020). Fifty years of
593 research on the Madden–Julian Oscillation: Recent progress, challenges, and perspectives.
594 *Journal of Geophysical Research: Atmospheres, 125*(17), e2019JD030911. https://doi.
595 org/10.1029/2019jd030911
596 Kalnay, E., Kanamitsu, M., Kistler, R., Collins, W., Deaven, D., Gandin, L., et al. (1996). The
597 NCEP/NCAR 40-Year Reanalysis Project. *Bulletin of the American Meteorological*
598 *Society*, *77*(3), 437–472. https://doi.org/10.1175/1520-
599 0477(1996)077<0437:TNYRP>2.0.CO;2
600 Kanamitsu, M., Kumar, A., Juang, H.-M. H., Schemm, J.-K., Wang, W., Yang, F., et al. (2002).
601 NCEP DYNAMICAL SEASONAL FORECAST SYSTEM 2000. *Bulletin of the*
602 *American Meteorological Society*, *83*(7), 1019–1038. https://doi.org/10.1175/1520-
603 0477(2002)083<1019:NDSFS>2.3.CO;2
604 Kao, H.-Y., & Yu, J.-Y. (2009). Contrasting eastern-Pacific and central-Pacific types of ENSO.
605 *Journal of Climate*, *22*(3), 615–632. https://doi. org/10.1175/2008jcli2309.1
606 Khouider, B., & Majda, A. J. (2008). Equatorial convectively coupled waves in a simple multi-
607 cloud model. *Journal of the Atmospheric Sciences*, *65*(11), 3376–3397.
608 https://doi.org/10.1175/2008JAS2752.1
609 Kikuchi, K. (2021). The Boreal Summer Intraseasonal Oscillation (BSISO): A Review. *Journal*
610 *of the Meteorological Society of Japan. Ser. II*, *99*(4), 933-972.
611 https://doi.org/10.2151/jmsj.2021-045

612 Kiladis, G. N., Dias, J., Straub, K. H., Wheeler, M. C., Tulich, S. N., Kikuchi, K., et al. (2014). A
613 Comparison of OLR and Circulation-Based Indices for Tracking the MJO. *Monthly*
614 *Weather Review, 142*(5), 1697–1715. https://doi.org/10.1175/MWR-D-13-00301.1
615 Kim, D., Kug, J.-S., & Sobel, A. H. (2014). Propagating versus Nonpropagating Madden–Julian
616 Oscillation Events. *Journal of Climate*, *27*(1), 111–125. https://doi.org/10.1175/JCLI-D-
617 13-00084.1
618 Kim, D., Kim, H., & Lee, M.-I. (2017). Why does the MJO detour the Maritime Continent
619 during austral summer? *Geophysical Research Letters*, *44*(5), 2579–2587.
620 https://doi.org/10.1002/2017GL072643
621 Klein, S. A., Soden, B. J., & Lau, N.-C. (1999). Remote sea surface temperature variations
622 during ENSO: Evidence for a tropical atmospheric bridge, *Journal of Climate*, *12*(4),
623 917‑932. https://doi.org/10.1175/1520-0442(1999)012%3C0917:RSSTVD%3E2.0.CO;2
624 Kottapalli, A., & Vinayachandran, P. N. (2022). On the weakening of northward propagation of
625 intraseasonal oscillations during positive Indian Ocean Dipole events. *Climate Dynamics*,
626 *59*(3), 915-938. https://doi.org/10.1007/s00382-022-06164-w
627 Krishnamurthy, V., & Shukla, J. (2008). Seasonal persistence and propagation of intraseasonal
628 patterns over the Indian monsoon region. *Climate Dynamics*, *30*(4), 353–369.
629 https://doi.org/10.1007/s00382-007-0300-7
630 Kumar, R., Pathak, R., Sahany, S., & Mishra, S. K. (2023). Indian summer monsoon simulations
631 in successive generations of the NCAR Community Atmosphere Model. *Theoretical and*
632 *Applied Climatology*, *153*(3), 977–992. https://doi.org/10.1007/s00704-023-04514-0

633 Lau, K.-M., & Chan, P. (1986). The 40–50 day oscillation and the El Niño/ Southern Oscillation:
634 A new perspective. *Bulletin of the American Meteorological Society*, *67*(5), 533–534.
635 https://doi.org/10.1175/1520-0477(1986)067,0533:TDOATE.2.0.CO;2
636 Lee, J.-Y., Wang, B., Wheeler, M. C., Fu, X., Waliser, D. E., & Kang, I.-S. (2013). Real-time
637 multivariate indices for the boreal summer intraseasonal oscillation over the Asian
638 summer monsoon region. *Climate Dynamics*, *40*(1), 493–509.
639 https://doi.org/10.1007/s00382-012-1544-4
640 Liang, P., Hu, Z.-Z., Ding, Y., & Qian, Q. (2021). The Extreme Mei-yu Season in 2020: Role of
641 the Madden-Julian Oscillation and the Cooperative Influence of the Pacific and Indian
642 Oceans. *Advances in Atmospheric Sciences*, *38*(12), 2040–2054.
643 https://doi.org/10.1007/s00376-021-1078-y
644 Liebmann, B., & Smith, C. A. (1996). Description of a Complete (Interpolated) Outgoing
645 Longwave Radiation Dataset. *Bulletin of the American Meteorological Society*, *77*(6),
646 1275–1277.
647 Lin, A., & Li, T. (2008). Energy Spectrum Characteristics of Boreal Summer Intraseasonal
648 Oscillations: Climatology and Variations during the ENSO Developing and Decaying
649 Phases. *Journal of Climate*, *21*(23), 6304–6320. https://doi.org/10.1175/2008JCLI2331.1
650 Lin, A., Li, T., Fu, X., Luo, J.-J., & Masumoto, Y. (2011). Effects of air–sea coupling on the
651 boreal summer intraseasonal oscillations over the tropical Indian Ocean. *Climate*
652 *Dynamics*, *37*(11), 2303–2322. https://doi.org/10.1007/s00382-010-0943-7
653 Liu, F., Li, T., Wang, H., Deng, L., & Zhang, Y. (2016). Modulation of boreal summer
654 intraseasonal oscillations over the western North Pacific by ENSO. *Journal of Climate*,
655 *29*(20), 7189–7201. https://doi.org/10.1175/JCLI-D-15-0831.1

Lu, W., & Hsu, P.-C. (2017). Factors controlling the seasonality of the Madden-Julian Oscillation. *Dynamics of Atmospheres and Oceans*, *78*, 106–120. https://doi.org/10.1016/j.dynatmoce.2017.04.002

Madden, R. A. (1986). Seasonal Variations of the 40-50 Day Oscillation in the Tropics. *Journal of the Atmospheric Sciences*, *43*(24), 3138–3158. https://doi.org/10.1175/1520-0469(1986)043<3138:SVOTDO>2.0.CO;2

Madden, R. A., & Julian, P. R. (1971). Detection of a 40–50 Day Oscillation in the Zonal Wind in the Tropical Pacific. *Journal of the Atmospheric Sciences*, *28*(5), 702–708. https://doi.org/10.1175/1520-0469(1971)028<0702:DOADOI>2.0.CO;2

Madden, R. A., & Julian, P. R. (1972). Description of Global-Scale Circulation Cells in the Tropics with a 40–50 Day Period. *Journal of the Atmospheric Sciences*, *29*(6), 1109–1123. https://doi.org/10.1175/1520-0469(1972)029<1109:DOGSCC>2.0.CO;2

Madden, R. A., & Julian, P. R. (1994). Observations of the 40–50-Day Tropical Oscillation—A Review. *Monthly Weather Review*, *122*(5), 814–837. https://doi.org/10.1175/1520-0493(1994)122<0814:OOTDTO>2.0.CO;2

Majda, A., & Stechmann, S. N. (2009). A simple dynamical model with features of convective momentum transport. *ournal of the Atmospheric Sciences*, *66*(2), 373–392. https://doi.org/10.1175/2008JAS2805.1

Michelangeli, P.-A., Vautard, R., & Legras, B. (1995). Weather Regimes: Recurrence and Quasi Stationarity. *Journal of the Atmospheric Sciences*, *52*(8), 1237–1256. https://doi.org/10.1175/1520-0469(1995)052<1237:WRRAQS>2.0.CO;2

Pillai, P. A., & Sahai, A. K. (2016). Moisture dynamics of the northward and eastward propagating boreal summer intraseasonal oscillations: possible role of tropical Indo-west

679 Pacific SST and circulation. *Climate Dynamics*, *47*(3), 1335–1350.
680 https://doi.org/10.1007/s00382-015-2904-7
681 Pohl, B., & Matthews, A. J. (2007). Observed changes in the lifetime and amplitude of the
682 Madden–Julian oscillation associated with interannual ENSO sea surface temperature
683 anomalies. *Journal of* Climate, *20*(11), 2659–2674. https://doi.org/10.1175/JCLI4230.1
684 Qiao, S., Chen, D., Wang, B., Cheung, H.-N., Liu, F., Cheng, J., et al. (2021). The Longest 2020
685 Meiyu Season Over the Past 60 Years: Subseasonal Perspective and Its Predictions.
686 *Geophysical Research Letters*, *48*(9), e2021GL093596.
687 https://doi.org/10.1029/2021GL093596
688 Ren, H.-L., Jin, F., Stuecker, M., & Xie, R. (2013). ENSO regime change since the late 1970s as
689 manifested by two types of ENSO. *Journal of the Meteorological Society of Japan.*
690 *Series II*, *91*(6), 835–842. https://doi.org/10.2151/jmsj.2013-608
691 Ren, H.-L., & Ren, P. F. (2017). Impact of Madden-Julian Oscillation upon winter extreme
692 rainfall in southern China: Observations and predict-ability in CFSv2. *Atmosphere*, *8*(10),
693 192. https://doi.org/10.3390/atmos8100192
694 Ren, H.-L., Wei, Y., & Zhao, S. (2023). Low-frequency variability in the real-time multivariate
695 MJO index: Real or artificial? *Journal of Climate*, *36*(7), 2073–2089.
696 https://doi.org/10.1175/jcli-d-22-0368.1
697 Ren, P., Ren, H.-L., Fu, J., Wu, J., & Du, L. (2018). Impact of boreal summer intraseasonal
698 oscillation on rainfall extremes in southeastern China and its predictability in CFSv2.
699 *Journal of Geophysical Research: Atmospheres*, *123*(9), 4423–4442. https://doi.
700 org/10.1029/2017jd028043

Ren, P., Kim, D., Ahn, M.-S., Kang, D., Ren, H.-L. (2021). Intercomparison of MJO column moist static energy and water vapor budget among six modern reanalysis products. *Journal of Climate*, *34*(8), 2977–3001. https:// doi: 10.1175/JCLI-D-20-0653.1..

Reynolds, R. W., Smith, T. M., Liu, C., Chelton, D. B., Casey, K. S., & Schlax, M. G. (2007). Daily High-Resolution-Blended Analyses for Sea Surface Temperature. *Journal of Climate*, *20*(22), 5473–5496. https://doi.org/10.1175/2007JCLI1824.1

Sabeerali, C. T., Ramu Dandi, A., Dhakate, A., Salunke, K., Mahapatra, S., & Rao, S. A. (2013). Simulation of boreal summer intraseasonal oscillations in the latest CMIP5 coupled GCMs. *Journal of Geophysical Research: Atmospheres*, *118*(10), 4401–4420. https://doi.org/10.1002/jgrd.50403

Saji, N. H., Goswami, B. N., Vinayachandran, P. N., & Yamagata, T. (1999). A dipole mode in the tropical Indian Ocean. *Nature*, *401*, 360-363. https://doi.org/10.1038/43854

Seiki, A., Nagura, M., Hasegawa, T., & Yoneyama, K. (2015). Seasonal onset of the Madden-Julian Oscillation and its relation to the southeatern Indian Ocean cooling. *Journal of the Meteorological Society of Japan. Ser. II*, *93A*,139-156. https://doi.org/10.2151/jmsj.2015-047

Shinoda, T., & Han, W. Q. (2005). Influence of the Indian Ocean dipole on atmospheric subseasonal variability. *Journal of Climate*, *18*(18), 3891-3909. https://doi.org/10.1175/JCLI3510.1

Slingo, J., Rowell, D., Sperber, K., & Nortley, F. (1999): On the predictability of the interannual behaviour of the Madden–Julian oscillation and its relationship with El Niño. *Quarterly Journal of the Royal Meteorological Society*, *125*(554), 583–609. https://doi.org/10.1002/qj.49712555411

724 Suhas, E., Neena, J. M., & Goswami, B. N. (2013). An Indian monsoon intraseasonal oscillations
725 (MISO) index for real time monitoring and forecast verification. *Climate Dynamics*,
726 *40*(11), 2605–2616. https://doi.org/10.1007/s00382-012-1462-5
727 Takasuka, D., & Satoh, M. (2021). Diversity of the Madden–Julian oscillation: Initiation region
728 modulated by the interaction between the intraseasonal and interannual variabilities.
729 *Journal of Climate*, 34(6), 2297–2318. https://doi.org/10.1175/jcli-d-20-0688.1
730 Vitart, F., Ardilouze, C., Bonet, A., Brookshaw, A., Chen, M., Codorean, C., et al. (2017). The
731 subseasonal to seasonal (S2S) prediction project database. *Bulletin of the American*
732 *Meteorological Society*, *98*(1), 163–173. https://doi.org/10.1175/bams-d-16-0017.1
733 Wang, B., & Rui, H. (1990). Synoptic climatology of transient tropical intraseasonal convection
734 anomalies: 1975–1985. *Meteorology and Atmospheric Physics*, *44*(1), 43–61.
735 https://doi.org/10.1007/BF01026810
736 Wang, B., & Chen, G. (2017). A general theoretical framework for understanding essential
737 dynamics of Madden–Julian oscillation. *Climate Dynamics*, *49*(7), 2309–2328.
738 https://doi.org/10.1007/s00382-016-3448-1
739 Wang, B., & Xie, X. (1996). Low-Frequency Equatorial Waves in Vertically Sheared Zonal
740 Flow. Part I: Stable Waves. *Journal of the Atmospheric Sciences*, *53*(3), 449–467.
741 https://doi.org/10.1175/1520-0469(1996)053<0449:LFEWIV>2.0.CO;2
742 Wang, B., & Xie, X. (1997). A Model for the Boreal Summer Intraseasonal Oscillation. *Journal*
743 *of the Atmospheric Sciences*, *54*(1), 72–86. https://doi.org/10.1175/1520-
744 0469(1997)054<0072:AMFTBS>2.0.CO;2
745 Wang, B., Liu, F., & Chen, G. (2016). A trio-interaction theory for Madden–Julian oscillation.
746 *Geoscience Letters*, *3*(1), 34. https://doi.org/10.1186/s40562-016-0066-z

747 Wang, B., Chen, G., & Liu, F. (2019). Diversity of the Madden-Julian Oscillation. *Science*
748 *Advances*, *5*(7), eaax0220. https://doi.org/10.1126/sciadv.aax0220
749 Wang, C. (2019). Three-ocean interactions and climate variability: a review and perspective.
750 *Climate Dynamics*, *53*(7), 5119–5136. https://doi.org/10.1007/s00382-019-04930-x
751 Wang, L., Li, T., Maloney, E., & Wang, B. (2017). Fundamental Causes of Propagating and
752 Nonpropagating MJOs in MJOTF/GASS Models. *Journal of Climate*, *30*(10), 3743–
753 3769. https://doi.org/10.1175/JCLI-D-16-0765.1
754 Wang, Y., Ren, H.-L., Wei, Y., Jin, F.-F., Ren, P., Gao, L., & Wu, J. (2022). MJO Phase Swings
755 Modulate the Recurring Latitudinal Shifts of the 2020 Extreme Summer-Monsoon
756 Rainfall Around Yangtse. *Journal of Geophysical Research: Atmospheres*, *127*(6),
757 e2021JD036011. https://doi.org/10.1029/2021JD036011
758 Wei, Y., Liu, F., Ren, H.-L., Chen, G., Feng, C., & Chen, B. (2022). Western Pacific
759 premoistening for eastward-propagating BSISO and its ENSO modulation. *Journal of*
760 *Climate*, *35*(15), 4979–4996. https://doi.org/10.1175/JCLI-D-21-0923.1
761 Wei, Y., & Pu, Z. (2021). Moisture variation with cloud effects during a BSISO over the eastern
762 Maritime Continent in a cloud-permitting-scale simulation. *Journal of the Atmospheric*
763 *Sciences*, *78*(6), 1869–1888. https://doi.org/10.1175/JAS-D-20-0210.1
764 Wei, Y., & Ren, H.-L. (2019). Modulation of ENSO on Fast and Slow MJO Modes during
765 Boreal Winter. *Journal of Climate*, *32*(21), 7483–7506. https://doi.org/10.1175/JCLI-D-
766 19-0013.1
767 Wei, Y., & Ren, H.-L. (2022). Distinct MJOs under the two types of La Niña. *Journal of*
768 *Geophysical Research: Atmospheres*, *127*(23), e2022JD037646.
769 https://doi.org/10.1029/2022JD037646

Wei, Y., & Ren, H.-L. (2024). MJO seasonality in its scale selection: Perspectives from space-time spectral analysis of moisture budget. *Journal of Geophysical Research: Atmospheres*, https://doi.org/10.1029/2023JD039645

Wei, Y., Ren, H.-L., Duan, W., & Sun, G. (2024). MJO-Equatorial Rossby Wave Interferences in the Tropical Intraseasonal Oscillation. *Climate Dynamics*, revised.

Wei, Y., Ren, H.-L., Xiang, B., Wang, Y., Wu, J., & Wang, S. (2023). Diverse MJO genesis and predictability. *Bulletin of the American Meteorological Society*, *1*(aop). https://doi.org/10.1175/BAMS-D-22-0101.1

Wheeler, M. C., & Hendon, H. H. (2004). An All-Season Real-Time Multivariate MJO Index: Development of an Index for Monitoring and Prediction. *Monthly Weather Review*, *132*(8), 1917–1932. https://doi.org/10.1175/1520-0493(2004)132<1917:AARMMI>2.0.CO;2

Wu, J., Ren, H.-L., Jia, X., & Zhang, P. (2023). Climatological diagnostics and subseasonal-to-seasonal predictions of Madden–Julian Oscillation events. *International Journal of Climatology*, *43*(5), 2449–2464. https://doi.org/10.1002/joc.7984

Yanai, M., Esbensen, S., & Chu, J.-H. (1973). Determination of Bulk Properties of Tropical Cloud Clusters from Large-Scale Heat and Moisture Budgets. *Journal of the Atmospheric Sciences*, *30*(4), 611–627. https://doi.org/10.1175/1520-0469(1973)030<0611:DOBPOT>2.0.CO;2

Yang, J., Liu, Q., Xie, S.-P., Liu, Z., & Wu, L. (2007). Impact of the Indian Ocean SST basin mode on the Asian summer monsoon. *Geophys. Res. Lett.*, *34*(2), L02708. https://doi.org/10.1029/2006GL028571

Yasunari, T. (1979). Cloudiness Fluctuations Associated with the Northern Hemisphere Summer Monsoon. *Journal of the Meteorological Society of Japan. Ser. II*, *57*(3), 227–242. https://doi.org/10.2151/jmsj1965.57.3_227

Zhang, C. (2013). Madden–Julian Oscillation: Bridging Weather and Climate. *Bulletin of the American Meteorological Society*, *94*(12), 1849–1870. https://doi.org/10.1175/BAMS-D-12-00026.1

Zhang, W., Huang, Z., Jiang, F., Stuecker, M. F., Chen, G., & Jin, F.-F. (2021). Exceptionally Persistent Madden-Julian Oscillation Activity Contributes to the Extreme 2020 East Asian Summer Monsoon Rainfall. *Geophysical Research Letters*, *48*(5), e2020GL091588. https://doi.org/10.1029/2020GL091588

Zhou, Z.-Q., Xie, S.-P., & Zhang, R. (2021). Historic Yangtze flooding of 2020 tied to extreme Indian Ocean conditions. *Proceedings of the National Academy of Sciences*, *118*(12), e2022255118. https://doi.org/10.1073/pnas.2022255118